POLITECNICO DI TORINO
Repository ISTITUZIONALE

Unraveling the effect of ZrO2 modifiers on the nature of active sites on AuRu/ZrO2 catalysts for furfural hydrogenation

(Article begins on next page)

28 April 2024

Unraveling the effect of ZrO$_2$ modifiers on the nature of active sites on AuRu/ZrO$_2$ catalysts for furfural hydrogenation

Sara Morandi[1], Maela Manzoli,[*,2] Carine E. Chan-Thaw,[3] Barbara Bonelli[4], Marta Stucchi,[3] Laura Prati, [3] Heike Störmer,[5] Wu Wang,[6] Di Wang,[6,7] Michael Pabel,[8] Alberto Villa[*,3]

[1] Dipartimento di Chimica and NIS – Interdepartmental Centre for Nanostructured Interfaces and Surfaces, Università degli Studi di Torino, Via P. Giuria 7, 10125 Torino, Italy.

[2] Dipartimento di Scienza e Tecnologia del Farmaco and NIS – Interdepartmental Centre for Nanostructured Interfaces and Surfaces, Università degli Studi di Torino, Via P. Giuria 9, 10125 Torino, Italy.

[3] Dipartimento di Chimica, Università degli Studi di Milano, via Golgi 19, I-20133 Milano, Italy

[4] Department of Applied Science and Technology and INSTM Unit of Torino Politecnico, Corso Duca degli Abruzzi 24, I-10129 Torino, Italy

[5] Laboratory for Electron Microscopy, Karlsruhe Institute of Technology, D-76128 Karlsruhe, Germany.

[6] Institute of Nanotechnology and [7] Karlsruhe Nano Micro Facility, Karlsruhe Institute of Technology, Hermann-von-Helmholtz-Platz 1, D-76344 Eggenstein-Leopoldshafen, Germany.

[8] Saint-Gobain NorPro A Division of Saint-Gobain Ceramic Materials GmbH Am Bahnhof D-56414 Steinefrenz Germany.

Corresponding authors

Alberto Villa

Email: Alberto.Villa@unimi.it

Maela Manzoli

Email: Maela.Manzoli@unito.it

Abstract.

Ru and AuRu nanoparticles were prepared by sol-immobilization methodology and deposited on different doped zirconia supports (ZrO_2, Y-ZrO_2 and La-ZrO_2). The catalysts were characterized by analytic transmission electron microscopy (TEM),Fourier Transform Infrared Spectroscopy (FTIR) in controlled atmosphere and X-ray Photoelectron Spectroscopy (XPS). TEM analysis showed that AuRu catalysts consist of Au-Ru particle aggregates with small Ru particles enriched on the Au surface. FTIR experiments of adsorbed CO and XPS analyses revealed that the presence of gold modifies the electronic properties of Ru, confirming the bimetallic nature of AuRu nanoparticles. The catalysts were tested in the furfural hydrogenation using isopropanol as hydrogen donor. The addition of Au to Ru did not significantly modify the activity and selectivity but enhanced the resistance to deactivation. The acid-base properties were monitored by acetonitrile adsorption followed by FTIR spectroscopy. It was shown that the acidity of the support greatly influences the selectivity. In particular, 71% selectivity to gamma-valerolactone was achieved over AuRu/ Y-ZrO_2, due to the modified acidic strength of Zr^{4+} sites on the Y-doped oxide.

1. Introduction

Furfural is traditionally produced from renewable lignocellulosic biomass and it is an ideal feedstock for the sustainable production of value-added chemicals and biofuels [1–3]. On the basis of indicators such as the raw material, cost and market potential, furfural is one of the top 10 biomass derived platform compounds [4]. Furfural catalytic hydrogenation yields a variety of products, such as furfuryl alcohol (FA), 2-methylfuran (MF) and tetrahydrofurfuryl alcohol [1–3]. FA is obtained from the hydrogenation of the carbonyl group, whereas MF forms through the further hydrogenolysis of FA (see Scheme 1). FA is used for the production of resins, or as non-reactive diluent for epoxy resins, modifier for phenolic and urea resins, solvent, or precursor for the synthesis of other chemicals [5]. It is also an important chemical intermediate for the manufacture of lysine, vitamin C, lubricant, dispersing agent and plasticizer. MF as well is an important intermediate in fine chemical, perfume and medical industry [6].
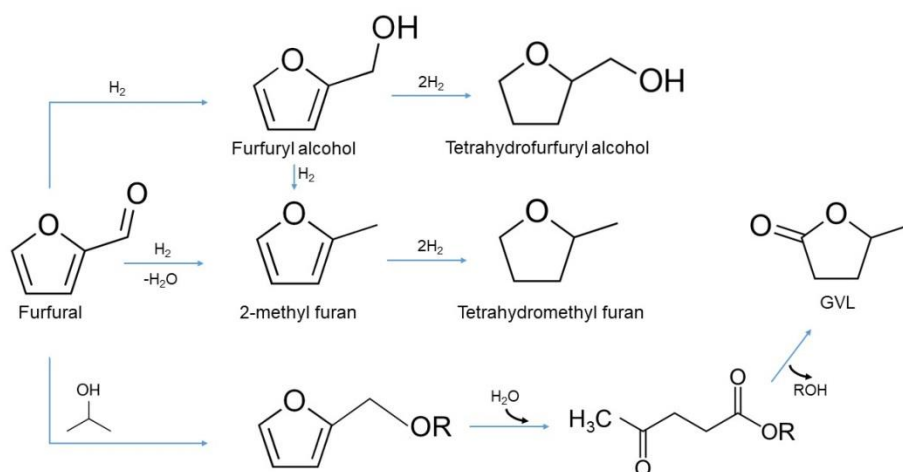
Scheme 1. Furfural hydrogenation pathways.

.

In addition, furfural can be converted also to other C_4 and C_5 chemicals, such as γ-valerolactone (GVL) [7,8] and pentanediols [9–11]. GVL is a 5 carbon cyclic ester with 1 oxygen atom in the ring. It is stable at normal conditions and its particular odor makes it suitable for the production of perfumes and food additives [12]. It is reactive enough for the synthesis of a variety of compounds including butene, valeric acid, and 5-nonanone, and, on the other hand, it is stable enough to be used as a solvent derived from biomass [13]. A possible route to obtain GVL from furfural involves the etherification of furfural with 2-propanol, used as solvent (Scheme 1) [14]. However, several side

reactions often occur simultaneously influencing the selectivity in a complex manner, depending on the catalyst employed.

The hydrogenation of furfural has been studied using mono- or bimetallic noble-metal catalysts mostly consisting of Pd and Ru [15–20]. Recently, the effect of the support in tuning the activity and selectivity in furfural hydrogenation has been object of study. Mikolajska et al., studying the activity of Pt deposited on different supports, i.e. SiO_2, γ-Al_2O_3, MgO, and TiO_2, showed high activity in furfural hydrogenation to furfuryl alcohol, but activity and selectivity were different considering the different supports [21]. Somorjai et al. carried out the hydrogenation of furfural over Pt nanoparticles supported on various mesoporous oxides to study catalytic selectivity by support effects, finding that the decarbonylation of furfural to furan was dominant [22]. Zhu et al. reported the activity of Au nanoparticles deposited on ZrO_2- ZSM-5 support, showing that the acidity of the support has an effect on activity and selectivity [7]. Moreover, also the use of a second metal, can be advantageous either for the activity or the selectivity in various liquid phase reactions, bringing a beneficial effect in terms of durability of the catalyst [23–26].

In this work, monometallic Ru and bimetallic AuRu nanoparticles prepared by sol immobilization were deposited on different ZrO_2 supports. The catalysts were tested in furfural hydrogenation using 2-propanol as H-donor. La-doped ZrO_2 and Y-doped ZrO_2 were selected on the basis of their different Lewis acidity, in order to correlate it with the overall catalyst structure, activity and selectivity for furfural hydrogenation.

2. Experimental

2.1 Materials

$NaAuCl_4 \cdot 2H_2O$ and $RuCl_3$ from Aldrich (99.99% purity), $NaBH_4$ (purity >96%) from Fluka and polyvinylalcohol (PVA) (Mw = 13,000–23,000, 87–89% hydrolyzed) from Aldrich were used. Gaseous nitrogen from SIAD were 99.99% pure. ZrO_2, La-ZrO_2 (La_2O_3 content= 88.9%,), Y-ZrO_2 (Y_2O_3 content= 7.3%) were provided by Saint-Gobain NorPro. The structural and textural properties of the commercial supports are summarized in Table 1. Pore size distribution and pore volume are reported in the SI (Figures SI-1).

Table 1. Structural and textural properties of the commercial supports.

Support	Crystalline phase	Specific surface area (m^2/g)	Pore volume (cm^3/g)
ZrO$_2$	tetragonal	140	0.30
Y-ZrO$_2$	tetragonal	115	0.33
La-ZrO$_2$	tetragonal	120	0.30

2.2 Catalyst Preparation

2.2.1 Monometallic catalysts

Supported Ru nanoparticles (NPs) were prepared by using a standard sol-immobilization procedure. Solid RuCl$_3$ was used to prepare solution of the desired concentration (5 x 10^{-4} M), to which aqueous solution of PVA (PVA/metal (wt/wt) = 0.5) was added. 0.1 M solution of NaBH$_4$ (NaBH$_4$/metal (mol/mol) = 8) was freshly prepared and added under stirring to form dark brown sol. PVA and NaBH$_4$ were used as protective agent and reducer, respectively. After 30 minutes, the colloidal solution was immobilized on the support under vigorous stirring. Before impregnation, the supports (1,5 mm pellets) were ground to obtain a powder (5 μ). The amount of support material required was calculated so as to give a final metal loading of 1 wt. %. The mixture was acidified to pH 2 by sulfuric acid before stirred for 60 minutes to accomplish full immobilization of the metal NPs on to the support. The slurry was filtered, washed thoroughly with distilled water, and dried overnight at 100°C. The final Ru loading was 1 wt. %.

The monometallic Au catalyst was prepared by adopting the same sol-immobilization procedure. In this case, NaAuCl$_4$•2H$_2$O was employed to obtain the starting solution (5 x 10^{-4} M) to be added to aqueous solution of PVA in order to have the same PVA/metal ratio (wt/wt) of 0.5. Then NaBH$_4$ solution (0.1 M) was freshly prepared and added (NaBH$_4$/metal (mol/mol) = 4) under stirring to form dark brown sol. After 30 minutes, the colloidal solution was immobilized on the support under vigorous stirring. The mixture was acidified to pH 2 by sulfuric acid before stirred for 60 minutes to accomplish full immobilization of the metal NPs on to the support. The slurry was filtered, washed thoroughly with distilled water, and dried overnight at 100°C. The final Au loading was 1 wt. %. The monometallic catalysts prepared were denoted as Ru/ZrO$_2$ and Au/ZrO$_2$.

2.2.2 Bimetallic AuRu catalysts

Supported AuRu NPs were prepared using the same standard sol-immobilization method employed for the monometallic samples. In this case, solid RuCl$_3$ and NaAuCl$_4$•2H$_2$O (Au/Ru 6/4 molar ratio) were used to prepare solution of the desired concentration (5 x 10^{-4} M), to which aqueous solution

of PVA (PVA/metal (wt/wt) = 0.5) was added. 0.1 M solution of $NaBH_4$ ($NaBH_4$/metal (mol/mol) = 8) was freshly prepared and added under stirring to form dark brown sol. After 30 minutes, the colloidal solution was immobilized on the support under vigorous stirring. The amount of support material required was calculated so as to give a final metal loading of 1 wt. %. The mixture was acidified to pH 2 by sulfuric acid before stirred for 60 minutes to accomplish full immobilization of the metal NPs on to the support. The slurry was filtered, washed thoroughly with distilled water, and dried overnight at 100°C. The final AuRu loading was 1 wt. %, with a Au:Ru molar ratio of 6:4. $AuRu/ZrO_2$, $AuRu/Y-ZrO_2$ and $AuRu/La-ZrO_2$ were prepared.

2.3 Methods

2.3.1 Catalytic tests

Furfural hydrogenation was performed at 150°C, using a stainless steel reactor (30 mL capacity), equipped with heater, mechanical stirrer, gas supply system and thermometer. Furfural solution (15 mL; 0.3 M in 2-propanol) was added into the reactor and the desired amount of catalyst (Furfural/metal ratio=500 mol/mol) was suspended in the solution. The pressure of the nitrogen was 5 bar. The mixture was let at 150 °C and mechanically stirred (1250 rpm). At the end of the reaction, the autoclave was cooled down to room temperature. Samples were removed periodically (0.2 mL) and HP 7820A gas chromato-graph equipped with a capillary column HP-5 30 m x 0.32 mm, 0.25 µm Film, by Agilent Technologies were employed. Authentic samples were analyzed to determine separation times. Quantitative analysis with external standard method (n-octanol) was used. Identification of products was performed using a Thermo Scientific Trace ISQ QD Single Quadrupole GC-MS equipped with a capillary column HP-5 30 m x 0.32 mm, 0.25 µm Film, by Agilent Technologies.

2.3.2 Characterization techniques

Surface area, porosity distribution and porosity volume of the commercial supports were determined by low temperature (T= -196 °C) N_2 adsorption using a Tristar II 3020 Micromeritics apparatus. Before measurement, samples were outgassed at T = 150 °C for 4 h in a nitrogen flux. Surface area and porosity distribution were calculated from nitrogen isotherms by B.E.T. and B.J.H. theories using the instrumental software (Version 1.03).

Preliminary transmission electron microscopy (TEM) and high resolution TEM (HR-TEM) measurements on monometallic Ru/ZrO_2 were carried out with a JEOL 3010-UHR instrument

operating at 300 kV and equipped with a LaB$_6$ filament. Digital micrographs were acquired by a Gatan (2k x 2k)-pixel Ultrascan1000 CCD camera and processed by Gatan digital micrograph. Before the measurements, to obtain a good dispersion of the sample particles and to avoid any modification induced by the use of a solvent, the powders were briefly contacted with the Cu grids coated with lacey carbon, resulting in the adhesion of some particles to the TEM grid by electrostatic interactions. Histograms of the particle size distribution were obtained by measuring ca. 300 particles on the TEM images, and the mean particle diameter (d_m) was calculated as $d_m = \Sigma d_i n_i / \Sigma n_i$, where n_i was the number of particles of diameter d_i. The counting was performed on electron micrographs obtained starting from 300,000x magnifications.

For the AuRu catalysts, high-angle annular dark field scanning transmission electron microscopy (HAADF-STEM) in combination with energy-dispersive X-ray spectroscopy (EDXS), using a FEI OSIRIS ChemiSTEM microscope operated at 200 kV acceleration voltage, was employed. Quantification of EDXS data was performed with the Bruker ESPRIT software. For quantification, only the Au:Ru ratio, using the Ru Kα-line and the Au Lα-line, was determined; additional elements were only used for background subtraction.

Absorption IR spectra were collected at room temperature (RT) with a Perkin-Elmer FT-IR system 2000 spectrophotometer equipped with a Hg-Cd-Te cryodetector, working in the range of wavenumbers 7200-580 cm^{-1} at a resolution of 2 cm^{-1} (number of scans 60). For IR analysis, the powder samples were pelletized in self-supporting disks (15-20 mg/cm^2) and placed in a home-made quartz IR cell allowing thermal treatments in vacuum or in controlled atmosphere and the recording of the spectra at RT.

Preliminary FTIR experiments of adsorbed CO were performed at liquid nitrogen temperature (LNT) on the samples previously outgassed at 100 °C for 30 minutes. As for the measurements carried out at RT, after the activation in vacuum at 100 °C, the samples were made to interact with CO (Praxair, > 99.997%) and 2-propanol (Carlo Erba, RPE) vapor on the base of the following steps: (i) admission of CO (15 mbar) at RT and subsequent outgassing at RT; (ii) admission of 2-propanol (5 mbar) at RT; (iii) thermal treatment at 100 °C in 2-propanol atmosphere; (iv) outgassing at RT, admission of CO (15 mbar) at RT. An IR spectrum was run at the end of each step. The above procedure allows to characterize the metal phase and the influence of the presence of 2-propanol.

In order to characterize the Lewis acid sites of the oxide supports, after the activation in vacuum at 100 °C, FTIR spectra were recorded at RT during the interaction with acetonitrile CH$_3$CN (Carlo Erba, RPE) at increasing pressure up to 2 mbar and subsequent outgassing at RT. Both ammonia

and pyridine were also employed, but they did not give reliable results due to the interaction with the PVA chains.

In the Figures, FTIR difference spectra are reported: the subtrahend spectrum is always that recorded at RT after the activation in vacuum at 100 °C. In this way, the surface species formed by the interaction with the probe molecules are better put in evidence.

X-ray Photoelectron Spectroscopy (XPS) analysis was carried out on a XPS PHI 5000 Versa probe apparatus, using a band-pass energy of 187.85 eV, a 45° take off angle and a 100.0 μm diameter X-ray spot size for survey spectra. High-resolution XP spectra were recorded in the following conditions: pass energy of 20 eV, resolution of 0.1 eV and step of 0.2 eV. Sample charging effects were eliminated by referring to the spectral line shift of the C 1 s binding energy (BE) value at 284.5 eV. XP-spectra were analyzed by means of a commercial software (CasaXPS, version 2.3.16).

3. Results and discussion

3.1 Catalytic activity and selectivity

Table 2 reports the activity, calculated as converted mols of furfural divided by mols of metal × hour (h^{-1}) and calculated after 15 minutes of reaction, and the selectivity. AuRu/ZrO$_2$ catalyst showed higher activity (410 h^{-1}) compared to the corresponding monometallic counterparts (342 and 9 h^{-1} for Ru/ZrO$_2$ and Au/ZrO$_2$, respectively). It is worth noting that the Au catalyst is almost inactive under these reaction conditions (Table 2). Moreover, the addition of Au to Ru has also an evident effect on the catalyst stability. Indeed, Ru/ZrO$_2$ rapidly deactivates after two hours of reaction, whereas AuRu/ZrO$_2$ shows 88% conversion after 5 hours (Figure 1). On the contrary, the presence of Au did not significantly influence the selectivity. Both catalysts produce furfuryl alcohol (52-54%), GVL (22-29%) and isopropyl-furfuryl ether in a similar quantity (10-16%, Table 2, Figure 2).

Table 2. Results of furfural hydrogenation carried out in the presence of mono- and bimetallic catalysts.

Catalyst[a]	Activity[b]	Selectivity (%)[c]						Average particle size (nm)
		Furfuryl alcohol	Tetrahydro furfuryl alcohol	2-methyl furan	2-methyl tetrahydro furan	GVL	Isopropyl-furfuryl ether	
Au/ZrO$_2$	9	-	-	-	-	-	-	
Ru/ZrO$_2$	342	52	-	5	-	22	16	2.0 ± 0.4
AuRu/ZrO$_2$	410	54	-	3	1	29	10	4.7 ± 0.8
AuRu/Y-ZrO$_2$	380	14	2	6	-	71	7	4.5 ± 0.6
AuRu/La-ZrO$_2$	430	84	-	-	-	9	6	5.3 ± 0.6
Au/ZrO$_2$ + Ru/ZrO$_2$	336	50	-	6	-	20	23	

[a] Reaction conditions: Furfural = 0.3 M; F/metal ratio=500 wt/wt, 150°C, 5 bar N$_2$, solvent 2-propranol.
[b] Converted mol (mol metal)$^{-1}$ h^{-1} calculated after 15 min of reaction.
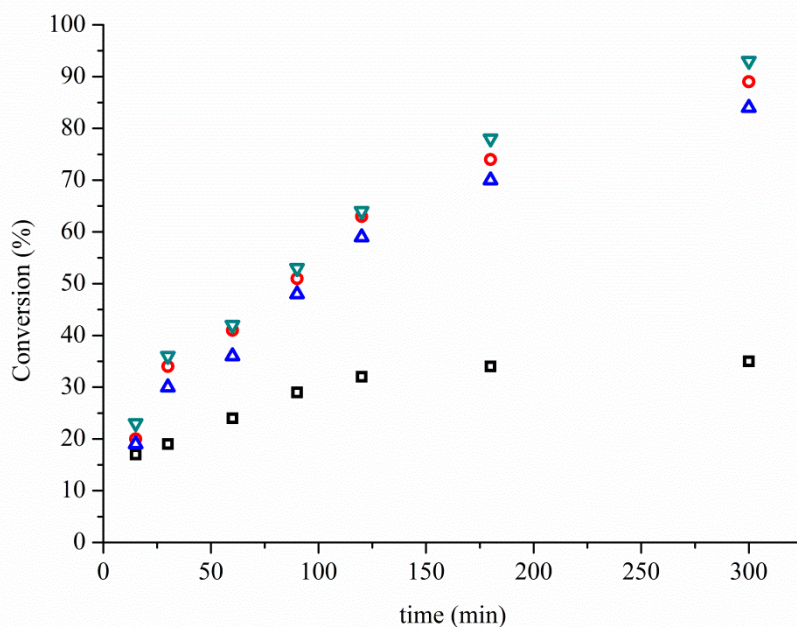[c] Selectivity calculated after 5 h of reaction

Figure 1. Reaction profile for monometallic Ru/ZrO$_2$ (black squares), and bimetallic AuRu/ZrO$_2$ (red circles), AuRu/Y-ZrO$_2$ (blue triangles) and AuRu/La-ZrO$_2$ (cyan triangles) catalysts.

AuRu nanoparticles were also deposited on Y- and La-functionalized ZrO$_2$ (Y-ZrO$_2$ and La-ZrO$_2$, respectively). In particular, the support did not affect significantly the initial activity (410, 380, and 430 h^{-1}, for AuRu/ZrO$_2$, AuRu/Y-ZrO$_2$ and AuRu/La-ZrO$_2$, respectively, Table 2) and the reaction profile (88%, 91%, and 83% conversion for AuRu/ZrO$_2$, AuRu/Y-ZrO$_2$ and AuRu/La-ZrO$_2$, respectively, Figure 1).

On the contrary, the support has a substantial influence on the selectivity, according to the results in Table 2 and as shown in Figure 2 in which the product distributions for Ru/ZrO$_2$ (section a), AuRu/ZrO$_2$ (section b), AuRu/Y-ZrO$_2$ (section c) and AuRu/La-ZrO$_2$ (section d) are reported. Indeed, AuRu/Y-ZrO$_2$ promoted the formation of GVL as main product (71%), whereas AuRu/La-ZrO$_2$ gives high selectivity to furfuryl alcohol (84%).
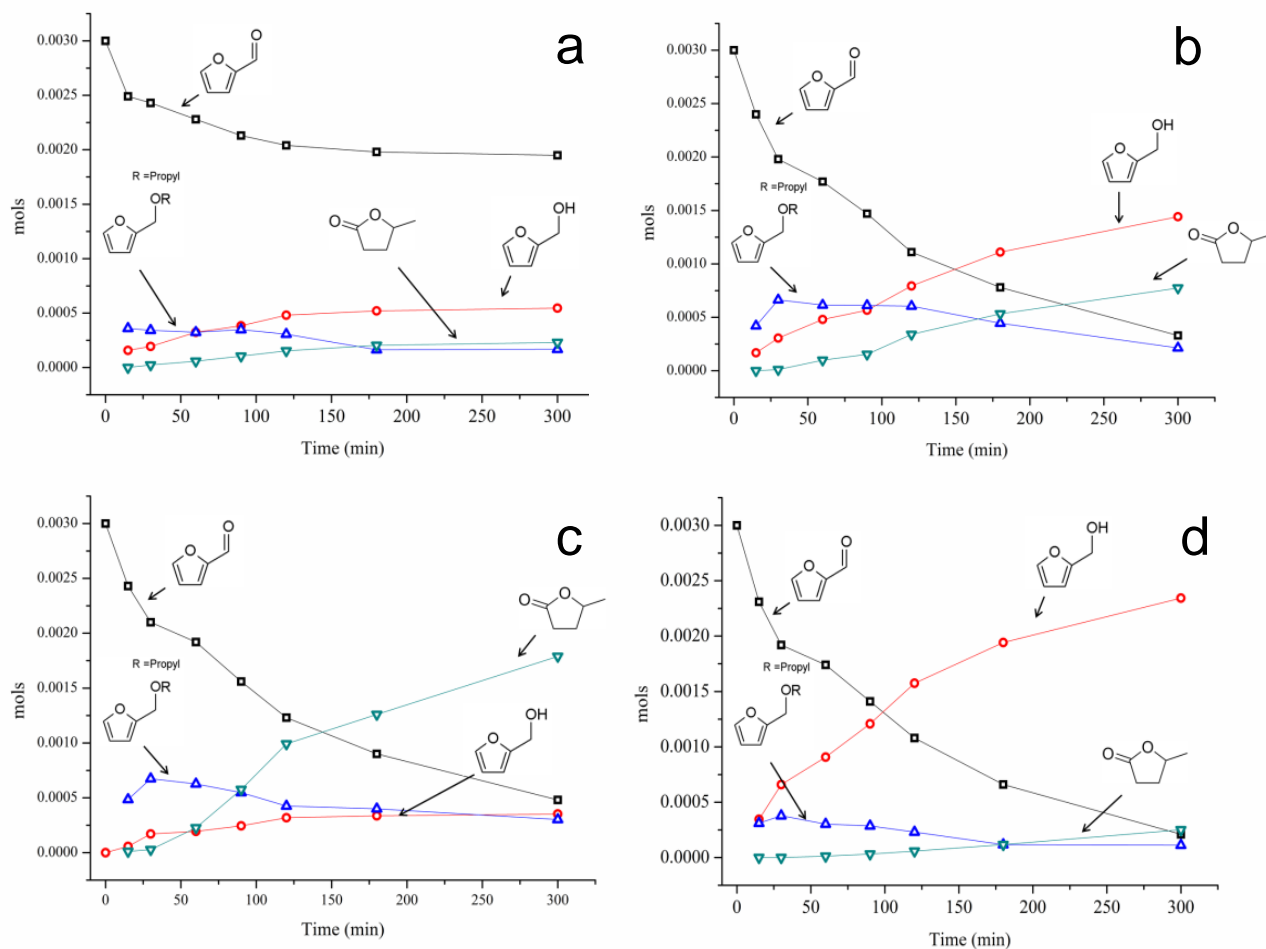

Figure 2. Product distribution for Ru/ZrO$_2$ (section a), AuRu/ZrO$_2$ (section b), AuRu/Y-ZrO$_2$ (section c) and AuRu/La-ZrO$_2$ (section d).

The stability of AuRu/Y-ZrO$_2$, which shows the highest selectivity to GVL, was evaluated. Recycling tests have been performed by filtering the catalyst after each run and reusing it without any pretreatment. Figure 3 showed that the catalyst is stable in terms of conversion and selectivity to GVL for 8 cycles.
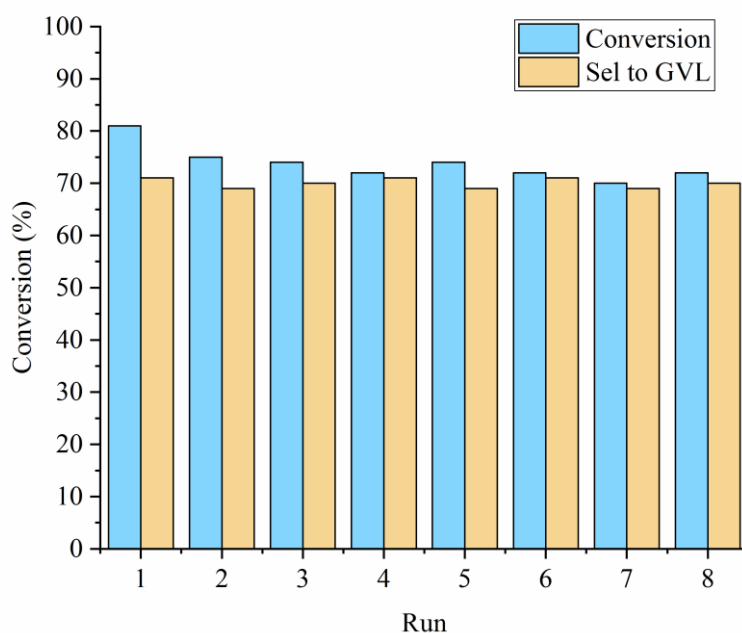

Figure 3. Stability tests performed using AuRu/Y-ZrO$_2$.

To understand the effect of the nanoparticle morphology and the surface chemistry of the support on the catalytic results, the catalysts have been extensively characterized using STEM-EDX spectrum imaging and FTIR spectroscopy of adsorbed probe molecules.

3.2 (Mono) and bimetallic supported nanoparticles: size and morphology

The monometallic Ru/ZrO$_2$ catalyst possesses a quite homogeneous distribution of Ru nanoparticles over the zirconia support, as shown by the HR-TEM characterization reported in Figure SI-2, section a. The average size of the Ru nanoparticles (highlighted by circles) is 2.0 ± 0.4 nm and the corresponding Ru particle size distribution is narrow (Table 1 and Figure SI-3a). The bimetallic catalysts were characterized by HAADF STEM imaging in combination with analytical measurements. The catalysts showed a narrow particle size distribution with an average particle size in the 4-5 nm range (Table 1 and Figure SI-3b and 3c). Based on the EDX signal of the Au-L and

Ru-K line, the distribution of the two metals within the bimetallic catalyst can be identified and quantified. Generally, the distribution of the catalyst particles is less homogeneous compared to the monometallic Ru catalyst. As can be seen from Figure 4, section a, particles tend to agglomerate. Quantitative EDX analysis (Figure 4, section b) on several such aggregate gives mean Au concentration of 61.1 ± 6 at.% and Ru 38.9 ± 4 at.%, in good agreement with the nominal value. Figure 4c shows quantified EDXS mapping (Au, red and Ru, green), indicating a considerable number of Ru NPs sitting on top of the big Au NP. The corresponding HAADF STEM image of the mapped particle is shown in Figure 4, section d. Similarly, when Y-ZrO$_2$ and La-ZrO$_2$ were used as supports, such configuration with small Ru particles sitting on the big Au particle was also observed (Figures SI-4 and SI-5, respectively). In addition, small Ru particles were also found distributing elsewhere on ZrO$_2$ support than in the vicinity of Au particles.
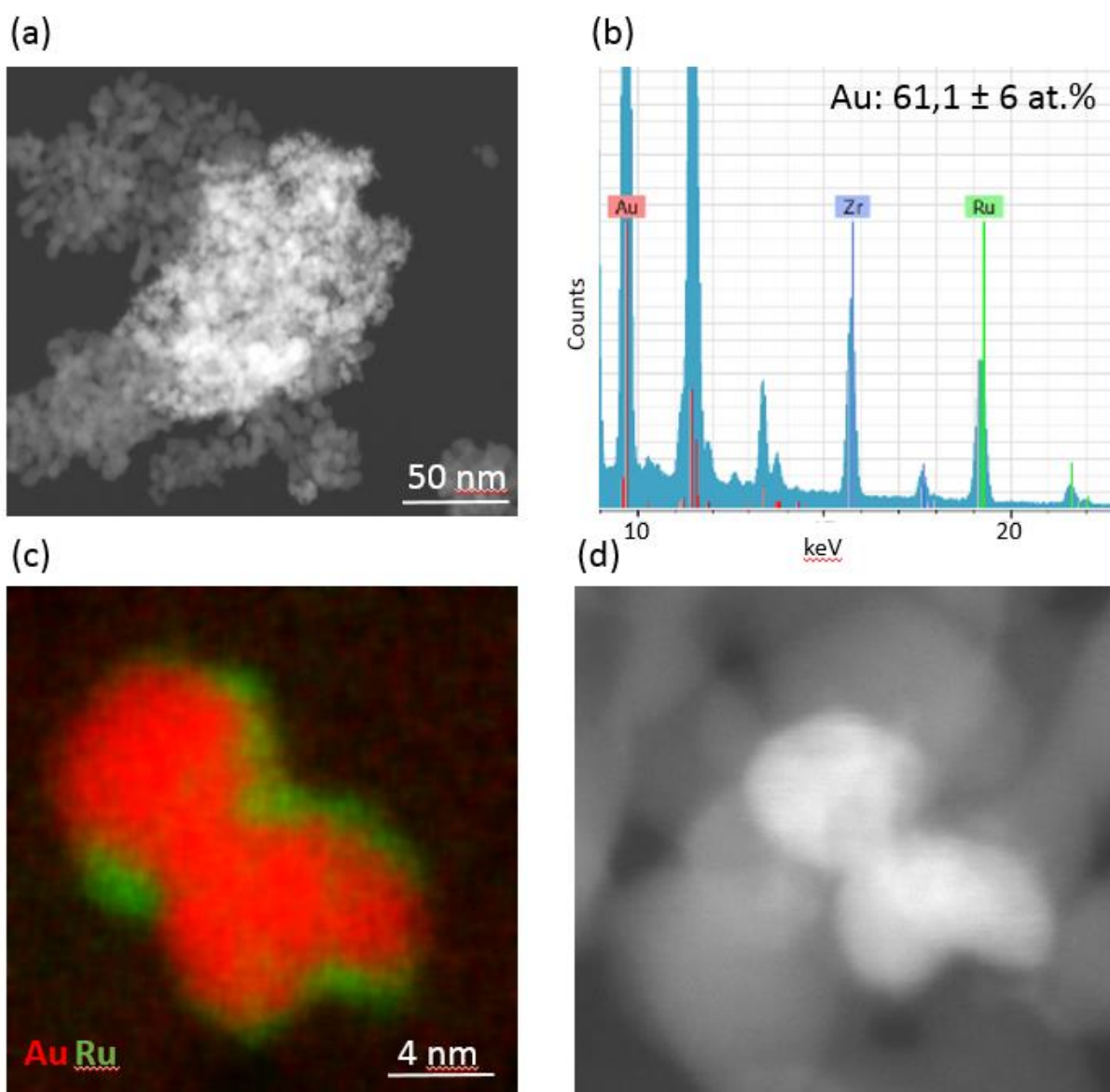
Figure 4. HAADF-STEM overview image of the AuRu/ZrO$_2$ sample (section a), EDX spectra of the Au-Lα and the Ru-Kα lines (section b), giving a mean Au concentration of 61.1 ±6 at.% (measurement of 10 different NP aggregates in the size of approximately 100 nm), quantified EDXS mapping (section c, Au,(red and Ru,green), showing the Ru NPs sitting on top of the Au NP, and corresponding HAADF image (section d).

3.3 Interaction between PVA and the support

To shed light on the interaction between the PVA chains and the supports, a comparison among the absorbance spectra of the catalysts submitted to outgassing at 100 °C for 30 minutes is shown in Figure 5b in the 1750-580 cm^{-1} spectroscopic range. In this region, rather defined bands related to the bending modes of CH$_2$ (1500-1200 cm^{-1}) and OH (1200-1000 cm^{-1}) groups of the PVA protecting agent are observed (Figure 5a). The intensity of these bands is correlated to the extent of the intra-chain interactions, which depends on the length and on the entangling of the chains. The band at 849 cm^{-1} is due to the C-O bending mode.
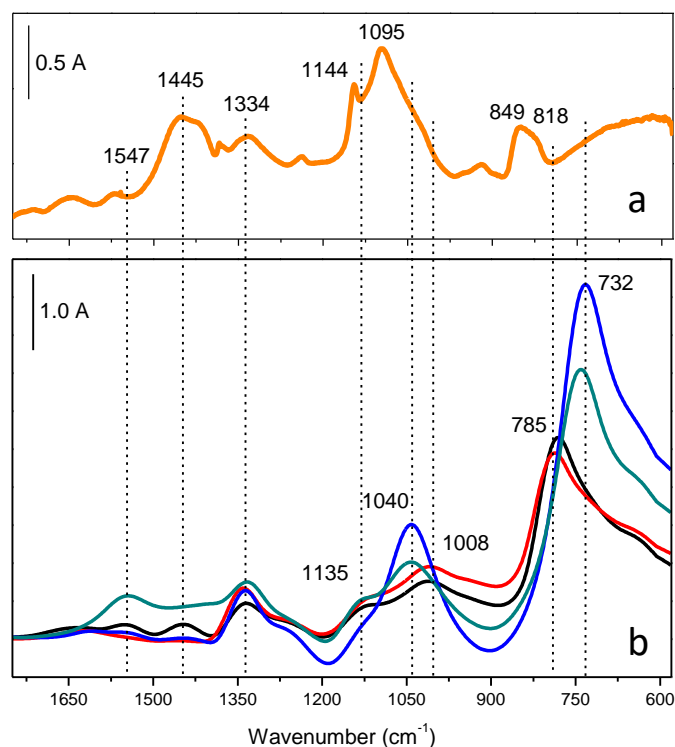

Figure 5. FTIR absorbance spectra of PVA in KBr (section a) and of monometallic Ru/ZrO$_2$ (black curve), bimetallic AuRu/ZrO$_2$ (red curve), AuRu/Y-ZrO$_2$ (blue curve) and AuRu/La-ZrO$_2$ (cyan curve) catalysts collected upon outgassing at 100 °C for 30 minutes (section b). The spectra in section b have been normalized on the weights of the pellets.

Upon interaction with the supports (Figure 5b), a strong modification of both position and relative intensity of these bands is observed. This is particularly evident for the absorption bands related to the bending modes of OH groups (1200-1000 cm^{-1}) and C-O bonds (900-600 cm^{-1}). A red shift is observed in both cases, whereas as for the C-O bending modes also a marked increase in intensity occurs. These features remark a strong interaction between the PVA and the zirconia support, which is particularly evident for Y- and La-modified supports. It can be therefore proposed that the mobility of the chains is affected by this interaction, depending on the acid-base properties of the support. In particular, a stronger interaction resulted into more spread PVA chains on the surface, possibly causing a higher exposure of the metallic sites.

3.4 Nature of the metal exposed sites and influence of 2-propanol

FTIR experiments of adsorbed CO at LNT were performed on the Ru/ZrO$_2$ catalyst after sample outgassing for 30 minutes at 100 °C. Such procedure allowed removing water from the catalyst surface without compromising the PVA protecting layer around the metal NPs. The spectra were collected after adsorption of 4 mbar CO and at decreasing CO pressure and the results are reported in Figure SI-6.

Basing on the behavior toward the pressure decrease in the OH stretching region reported in section a of Figure SI-6, the main peak at 2160 cm^{-1} is assigned to CO in interaction with the OH groups of zirconia (peak at 3557 cm^{-1}) and, possibly with OH of PVA as well (broad band at 3221 cm^{-1}), and to CO on coordinatively unsaturated Zr^{4+} sites [27], whereas the shoulder at 2177 cm^{-1} is due to CO on coordinatively unsaturated Zr^{4+} sites with different Lewis acid strength [28]. In addition, the very weak component at 2000-2050 cm^{-1}, not reversible to the outgassing and highlighted in the inset in Figure SI-6, is attributed to CO adsorbed on isolated Ru^0 sites [29,30].

The very low intensity of the absorption related to the Ru carbonyl is due to the poor availability of the Ru sites, despite the well-known high stability of these species. Indeed, the PVA protecting agent is able to inhibit the CO adsorption on the metal sites at low temperature. Therefore, the FTIR experiments of CO adsorption have been performed at RT on the samples activated at 100 °C. The comparison among the spectra collected after CO admission at RT and subsequent outgassing at the same temperature on monometallic Ru/ZrO$_2$ (black curve), bimetallic AuRu/ZrO$_2$ (red curve), AuRu/Y-ZrO$_2$ (blue curve) and AuRu/La-ZrO$_2$ (cyan curve) catalysts is reported in Figure 6.

Bands at 2125, 2050 and 1995 cm^{-1} are formed after adsorption of 15 mbar of CO and outgassing at RT on the Ru/ZrO$_2$ catalyst (black curve). These species are immediately produced after CO admission and do not disappear upon outgassing at RT. The bands at 2125 and 2050 cm^{-1} are

assigned to the asymmetric and symmetric stretching of twin CO molecules adsorbed on Ru^{n+} oxidized sites, with n = 2 or 3, produced by the dissociation of other CO molecules on some Ru^0 sites [31]. The band at 1995 cm^{-1} is due to CO molecules adsorbed on Ru^0 sites [29,30]. This behaviour suggests the presence of a fraction of highly dispersed and reactive Ru^0 sites, which are able to dissociate CO, and a fraction of Ru^0 centres, which are less-reactive toward CO decomposition.

When CO is adsorbed on the bi-metallic AuRu/ZrO$_2$ catalyst (red curve) a decrease in intensity of the band at 1995 cm^{-1}, accompanied by a shift to 2005 cm^{-1}, and by a small increase in intensity of the components at 2050 and at 2125 cm^{-1} are observed. It is well known that Ru carbonyls are extremely more stable than gold carbonyls, which were not observed on these samples. These spectroscopic features indicate that in the presence of gold a modification of the electronic properties of Ru took place, indeed the amount of less-reactive Ru^0 centres is diminished and the frequency of the related carbonyls is blue-shifted, whereas the amount of highly dispersed and reactive Ru^0 sites is rather increased. The modification of the electronic properties of Ru is the result of the close contact with Au, as evidenced by HAADF-STEM analysis. In the case of AuRu/La-ZrO$_2$ (cyan curve) and of AuRu/Y-ZrO$_2$ (blue curve) the increase in intensity of all the carbonyl bands put in evidence a role of the La or Y dopant. For the dopants, it can be proposed a role in promoting the interaction between the zirconia support and the PVA molecules, resulting in an enhanced availability of Ru sites.
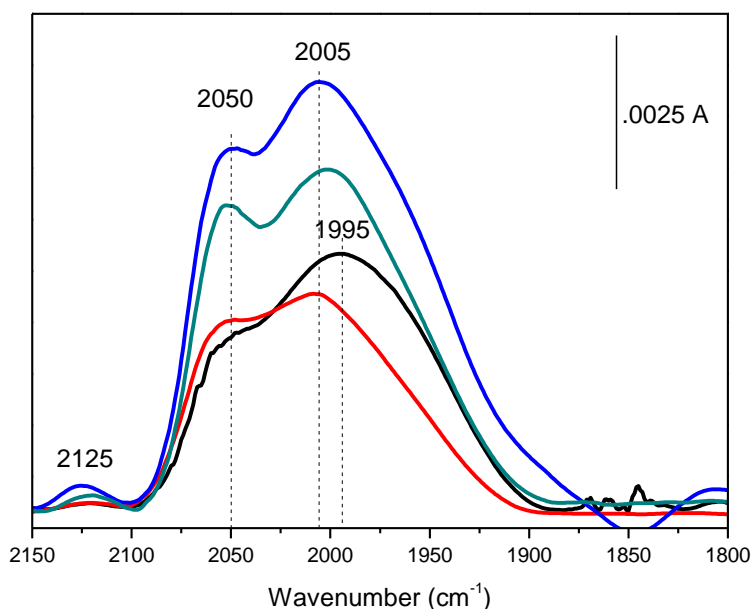

Figure 6. FTIR difference spectra collected upon the adsorption of 15 mbar CO at RT and subsequent outgassing at RT on monometallic Ru/ZrO$_2$ (black curve), and bimetallic AuRu/ZrO$_2$

(red curve), AuRu/Y-ZrO$_2$ (blue curve) and AuRu/La-ZrO$_2$ (cyan curve) catalysts. The spectra have been normalized on the weights of the pellets.

After CO adsorption experiments, the catalysts were further submitted to (i) admission of 2-propanol (5 mbar) at RT, (ii) thermal treatment at 100 °C in 2-propanol atmosphere in order to promote the interaction between the solvent and the PVA, further outgassing at RT, and (iii) re-admission of CO (15 mbar) at RT. With such experimental procedure, the effect of the PVA protecting agent on the availability of the Ru sites in contact with the reaction solvent was investigated. The results are summarized and compared in the carbonyl stretching region in Figure 7. In this Figure, the bold curves are the same as those commented and reported in Figure 6; on this situation, the admission of 2-propanol at RT (dashed curves) causes a redistribution of the carbonyl species bonded to Ru sites for all the samples. It is reasonable to hypothesize that 2-propanol interacts with PVA, making the Ru sites previously hidden by PVA chains accessible. On the basis of the vibration frequencies, it is possible to assert that the new available sites are Ru^0 sites. However, carbonyls rearrange on the metal surface, giving carbonyl species with vibration frequencies markedly lower than those evidenced before 2-propanol admission. This effect can be related to a spreading of CO on Ru^0: isolated carbonyls show the singleton frequency that is lower than that related to neighboring CO, which give dipole-dipole coupling. Typically, this coupling blue-shifts the vibration frequency with respect to the singleton one for carbonyls bonded to metals for which prevails the π back-donation, such as Ru [32].

Ru^{n+} carbonyls   Ru^0 carbonyls   Isolated Ru^0 carbonyls

.01 A

a

b

c

d

Wavenumber (cm⁻¹)

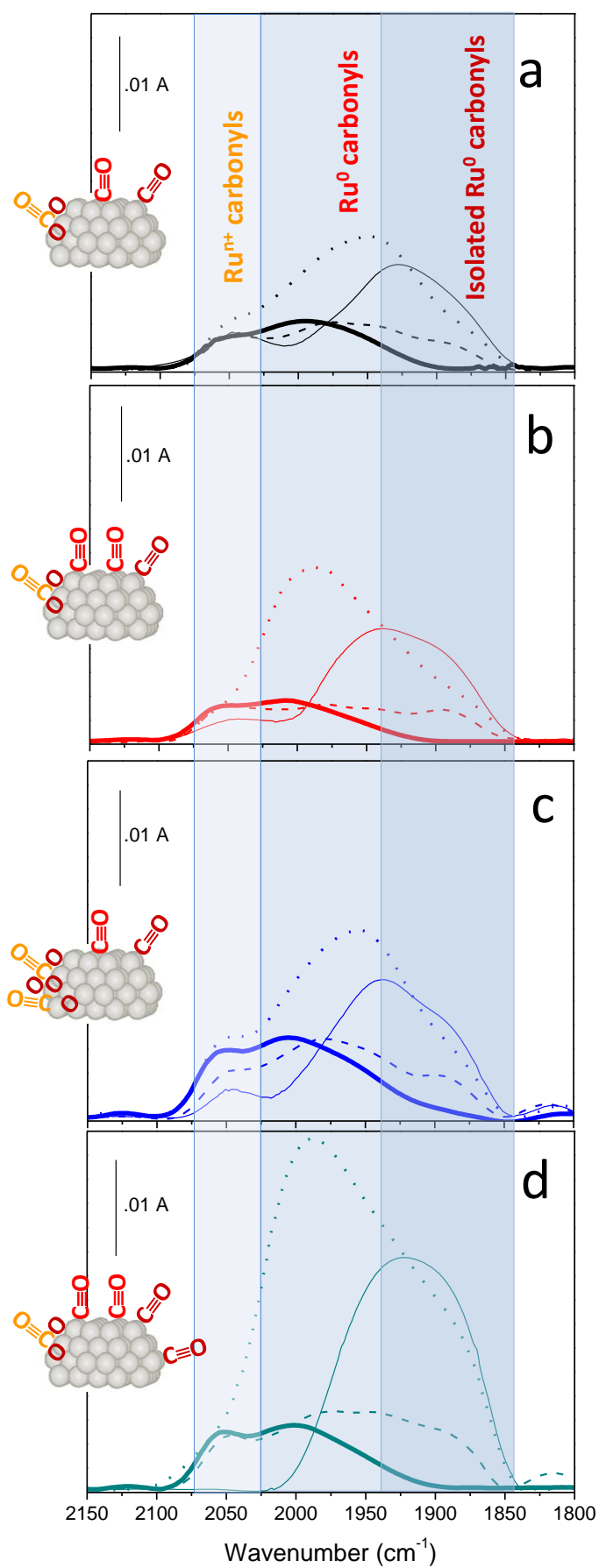2150   2100   2050   2000   1950   1900   1850   1800

Figure 7. FTIR difference spectra collected upon adsorption of 15 mbar CO at RT and subsequent outgassing at RT (bold curves), admission of 2-propanol (5 mbar) at RT (dashed curves), thermal treatment at 100 °C in 2-propanol atmosphere (fine curves) and further admission of CO (15 mbar) at RT after preliminary outgassing at the same temperature (dotted curves) on monometallic Ru/ZrO_2 (section a), and bimetallic $AuRu/ZrO_2$ (section b), $AuRu/Y-ZrO_2$ (section c) and $AuRu/La-ZrO_2$ (section d) catalysts. Sketches of the different Ru carbonyls are displayed in each section.

After treatment at 100 °C (fine curves) the amount of isolated Ru^0 carbonyls increases for all the samples. This can be related to the higher thermal energy that: (i) favors the motion and the spreading of carbonyls on Ru^0 sites; (ii) rises the amount of accessible Ru^0 sites by increasing the PVA chains mobility and by favoring the reduction by CO of Ru^{n+} sites . The reduction of Ru^{n+} sites is particularly evident for the bimetallic catalysts and is complete for the $AuRu/La-ZrO_2$, for which the amount of isolated carbonyls is markedly higher than that observed for the other samples: this can be ascribed to the presence of La, which reasonably makes stronger the interaction between the support and the PVA chains, causing the formation of a higher amount of accessible Ru^0 sites.

On the situation evidenced by fine curves in Figure 7, CO re-admission (dotted curves) simply causes an increase in the amount of adsorbed CO on Ru^{n+} (formed again by the dissociation of CO on Ru^0 sites at RT) and Ru^0 sites made available by the opening of PVA chains: the increase amount of carbonyls causes an increase in their surface density. As a consequence, the dipole-dipole coupling between them brings to a general blue-shift of the broad band related to CO on Ru^0.

Bimetallic particles are characterized by peculiar catalytic properties in terms of activity and selectivity, on which both electronic effects [33] and support interactions play a role.[34] The XPS technique allows studying such interactions. In bimetallic nanoparticles, the presence of gold usually promotes the oxidation of the other metal.[34,35] In this frame, Olmos et al. [35] reported that the formation of $Pd^{\delta+}$ species was favored on bimetallic Au-Pd catalysts supported on mixed ceria-zirconia.

As detailed in Table 3, the XPS $4f_{7/2}$ line of Au was found at 84.0, 83.8 and 83.9 eV for $AuRu/ZrO_2$, $AuRu/La-ZrO_2$ and $AuRu/Y-ZrO_2$ catalysts, respectively, i.e. at BE values typical of bulk Au^0 species.[36] According to the literature, when strong interactions take place with the support a decrease in the BE of the $4f_{7/2}$ line is observed, whereas here the $4f_{7/2}$ line position is nearly constant. Nonetheless, the measured BE values were very close to that of bulk Au (BE = 83.9 eV),[36] and higher with respect to the BE measured by Zhang et al [37] for Au nanoparticles interacting with ZrO_2 (BE = 83.5 eV). Such feature well agrees with the presence of large Au particles (decorated by small Ru nanoparticles) observed by HAADF STEM.

Element	Au	La	Y	Zr	Ru		O	
Line \ Sample	4f $_{7/2}$ BE (eV)	3d BE (eV) La_2O_3 / 3d BE (eV) $La_2(CO_3)_3$	3d$_{5/2}$ BE (eV) / 3d$_{3/2}$ BE (eV)	3d$_{5/2}$ BE (eV) / 3d$_{3/2}$ BE (eV) [FHWM]	3d$_{5/2}$ BE (eV) [at. %]		1s BE (eV) [at. %]	
					Ru^0	Ru^{n+}	O^{2-}	OH$^-$
Ru/ZrO$_2$	-		-	182.3 / 184.7 [1.4]	279.9 [16.0]	280.6 [84.0]	530.1 [62.4]	531.6 [37.6]
AuRu/ZrO$_2$	84.0		-	182.4 / 184.8 [1.4]	-	280.9 [100]	530.2 [68.4]	531.8 [31.7]
AuRu/La-ZrO$_2$	83.8	834.8-839.1 / 833.7-837.1	-	182.4 / 184.4 [1.3]	-	280.6 [100]	530.2 [71.5]	531.8 [28.5]
AuRu/Y-ZrO$_2$	83.9		157.2 / 159. 2	182.4 / 184.8 [1.4]	-	280.6 [100]	530.1 [70.6]	531.9 [29.4]

Concerning the XPS study of Ru species, curve-fitting procedures of the Ru 3d lines on different types of support are usually hampered by the presence of adventitious carbon[39,40] and, unfortunately, here the presence of PVA further complicated the interpretation of the Ru 3d lines.

Figure 8 reports the high-resolution XP spectra of the Ru 3d range for Ru/ZrO_2 (section a) and $AuRu/ZrO_2$ (section b), along with the curve fitting results concerning the $3d_{5/2}$ line. The spectra of $AuRu/Y-ZrO_2$ and $AuRu/La-ZrO_2$ (not reported for the sake of brevity) display quite similar features with respect to that of $AuRu/ZrO_2$. Notwithstanding the aforementioned problems, in the absence of Au the 3d line was satisfactorily curve fitted with two components, whereas with the Au-containing catalysts, only one component was present, due to oxidized species (referred to as Ru^{n+} in Table 3, where atomic percentages of Ru^0 and Ru^{n+} are also reported for all the studied samples).
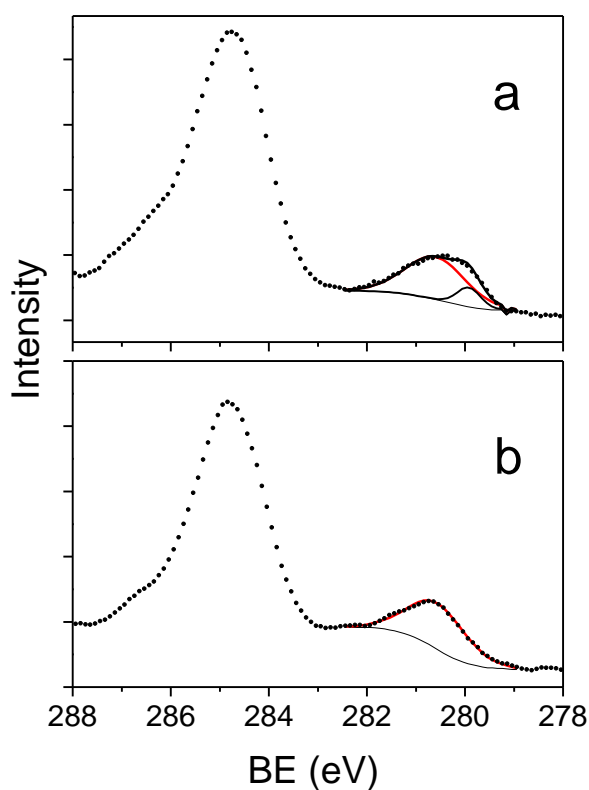
Figure 8. Ru 3d XP spectra (circles) for the samples Ru/ZrO_2 (a) and $Au-Ru/ZrO_2$ (b), along with the curve-fits. In both sections, the red line is the peak corresponding to the Ru^{n+} species, whereas in section (a) the peak of Ru^0 species is also reported as a black-line.

In agreement with the literature and the FTIR results discussed previously, in the presence of gold, surface ruthenium species are more easily oxidized, as it happens with Au-containing bimetallic

catalysts. Accordingly, such a facile oxidation of ruthenium is accompanied by an increased amount of O^{2-} with respect to OH^- ones (Table 3).

Concerning the support, either pure or doped with La or Y, the Zr $3d_{3/2}$ peak was very sharp with the four catalysts, as shown by the FHWM values reported in the Table 3, finally excluding the formation of zirconium suboxide,[41] both in the pure and doped samples. According to the literature, the Δ_{BE} between the BE of the Zr 3d $_{5/2}$ line and the BE of the O 1s line can be used to figure out whether a change in the oxidation state of Zr is occurring: here, the Δ_{BE} was 345.3 eV with the $AuRu/Y/ZrO_2$ sample and 345.4 eV with the other three samples, further confirming that the oxidation state of Zr was not changing by effect of the other metals present there.[41]

As for the two dopants, the high resolution spectrum of Y 3d was satisfactorily curve-fitted with one component (Table 3): the $3d_{5/2}$ line of yttrium at BE = 157.2 eV is typical of Y^{3+} species, for which the $3d_{5/2}$-$3d_{3/2}$ spin-orbit splitting is 2.05 eV and, accordingly, the $3d_{5/2}$ line is at 159.2 eV. The BE values are slightly higher than those reported for the Y $3d_{5/2-3/2}$ doublet in Y_2O_3 (i.e. 156.8 and 158.9 eV[42], although the positive chemical shift is small, it could be due to the interaction with slightly more electronegative Zr ions.[43]

The La $3d_{5/2}$ line (Table 3) was instead satisfactorily curve-fitted with two components (both further split by multiplet splitting), respectively ascribed to La_2O_3 (834.8-839.1 eV, with $\Delta BE = 4.3$ eV) and to $La_2(CO_3)_3$ (833.7 eV and 837.1 eV $\Delta BE = 3.4$), indicating also the occurrence of carbonate species, as expected in the presence of lanthanum.[44]

3.5 On the Lewis acid sites of the supports

The strength of the surface Lewis acid sites was characterized by acetonitrile adsorption followed by FTIR spectroscopy. On oxidic surfaces acetonitrile molecules are usually N-bonded to cationic sites, thanks to an electron pair in anti-bonding orbital. In general, both adsorbed and free acetonitrile molecules exhibit, in the C≡N stretching region, a couple of bands, which can be assigned to the $\nu(C≡N)$ fundamental mode, split by the coupling with the $\nu(C-C)+\delta_{asym.}(CH_3)$ combination (Fermi resonance) [45]. As known, the blue shift of the bands observed for the adsorbed molecules with respect to the bands observed for liquid acetonitrile (2292, 2254 cm^{-1}) depends on the electron withdrawing power of the adsorbing cationic site and can be taken as a measure of the Lewis acidity of the cationic site itself [46].

In Figure 9 the spectra recorded after admission and subsequent outgassing of CH_3CN at RT were reported in the C≡N stretching region. The spectra show: (i) a couple of bands for the $AuRu/ZrO_2$ catalyst (red curve) at 2318 and 2287 cm^{-1}; (ii) a couple of bands for the $AuRu/Y-ZrO_2$ catalyst

(blue curve) at 2315 and 2282 cm^{-1}; (iii) two couples of bands for the AuRu/La-ZrO$_2$ catalyst (cyan curve) at 2318, 2287 cm^{-1} and 2307, 2270 cm^{-1}. The presence of two couples of bands for this last sample put in evidence the presence of two kinds of Lewis acid sites. In particular, the bands at 2318 and 2287 cm^{-1}, the same observed for the AuRu/ZrO$_2$ catalyst, are assigned to Zr^{4+} sites; the bands at 2307 and 2270 cm^{-1} are assigned to La^{3+} sites. By comparing the relative position of the two couples of bands, it is possible to put in evidence that La^{3+} sites show lower acidic strength than Zr^{4+} sites. This finding makes the AuRu/La-ZrO$_2$ catalyst the less acidic one. The low acidic character can be related to the lowest selectivity to GVL shown by AuRu/La-ZrO$_2$, whose reactivity is mainly limited to furfuryl alcohol formation.
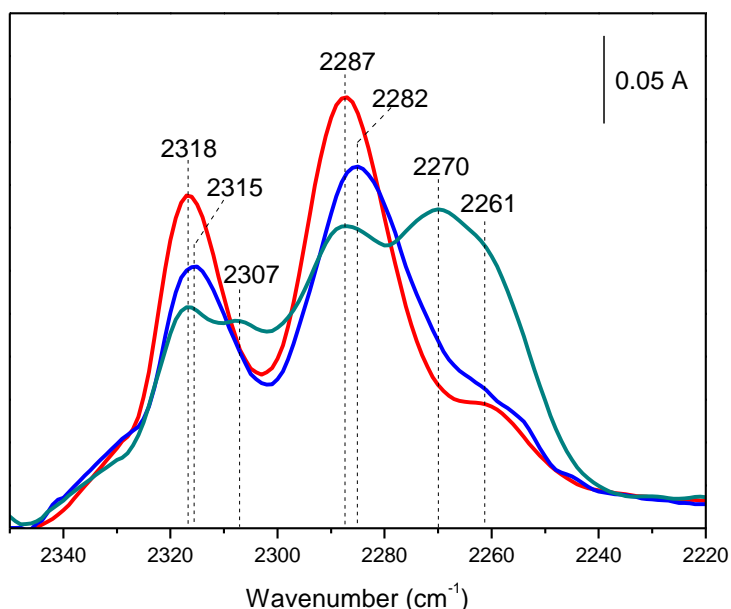
Figure 9. FTIR difference spectra collected upon the adsorption of 2 mbar CH$_3$CN at RT on bimetallic AuRu/ZrO$_2$ (red curve), AuRu/Y-ZrO$_2$ (blue curve) and AuRu/La-ZrO$_2$ (cyan curve) catalysts. The spectra have been normalized on the weights of the pellets and on the specific surface areas of the supports.

Differently from La, the introduction of Y does not cause the appearance of an additional couple of bands along with that of Zr^{4+} sites. However, the bands at 2315 and 2282 cm^{-1} related to Zr^{4+} for the AuRu/Y-ZrO$_2$ catalyst are at wavenumbers quite lower with respect to that observed for AuRu/ZrO$_2$: this finding put in evidence that Zr^{4+} sites on the Y-doped oxide show lower acidic strength than on pure ZrO$_2$. The modified acidic strength of Zr^{4+} sites could be the key for the high selectivity of the AuRu/Y-ZrO$_2$ catalyst to GVL: as a matter of fact, Lewis acidity is necessary to

drive the reaction to the GVL formation [47,48]. However, the mean acidity strength of AuRu/La-ZrO$_2$ is not enough and that of AuRu/ZrO$_2$ does not guarantee a high conversion to GVL, which is reached with a Lewis acidity modified by Y^{3+}.

Finally, the component observed at 2261 cm^{-1} for all the catalysts is associated with physisorbed acetonitrile; the other band of the Fermi couple, expected at about 2290 cm^{-1}, is overlapped to the modes of coordinated acetonitrile.

3.6 Structure activity relationships

The first observation is that the addition of gold, that did not show any activity under our reaction conditions, improved both activity and stability of the Ru catalyst. For all bimetallic catalysts, HAADF STEM coupled with EDX mapping showed similar morphology of the metal phase, which is constituted mainly by big Au nanoparticles in contact with small Ru nanoparticles, appearing deposited on top of the gold ones. Such peculiar morphology reasonably enhanced the stability of the metal phase up to 5 hours. Indeed, spectroscopic evidence of a strong interaction between the two metals is provided, since a modification of the electronic properties of Ru took place in the presence of gold. Moreover, a modification occurred also at the catalyst surface, because the amount of less-reactive Ru^0 centres is diminished, whereas the amount of highly dispersed and reactive Ru^0 sites is enhanced. These sites were shown to be fully accessible by 2-propanol, that is able to open the PVA chains which protect the metal sites. To verify the synergistic effect of AuRu bimetallic particles, a physical mixture of Au/ZrO$_2$ and Ru/ZrO$_2$ with a Au:Cu ratio of 6:4 was tested (Table 1). Normalizing the activity by the amount of Ru, it was possible to demonstrate that the physical mixture has a similar activity than pure Ru/ZrO$_2$, confirming that the synergistic effect occurs only when bimetallic particles are formed.

Moreover, it was shown that already at 100 °C the PVA chain mobility is enhanced as well as the amount of accessible Ru^0 sites, which results in an improved capability to activate 2-propanol. This is particularly evident in the case of the AuRu/La-ZrO$_2$ catalyst in which the presence of La promotes the interaction between the support and the PVA chains, resulting in higher accessibility of the Ru^0 sites, in agreement with the highest activity showed by AuRu/La-ZrO$_2$.

Interestingly, the presence of Au had almost no effect on the selectivity, because AuRu nanoparticles lead to the selective production of FA or GVL, depending on the strength of the Lewis acid sites of the supports. In particular, 71 % GVL and 84 % FA were formed on AuRu/Y-ZrO$_2$ and AuRu/La-ZrO$_2$, respectively. It can be proposed that furfural is converted into FA through hydrogen transfer promoted by the metal sites (see Scheme 2). Previous FTIR analyses pointed out

that furfural interact mainly through its carbonyl group with the surface of gold catalysts through different interactions involving several geometries of the molecule and possibly different kind of exposed sites. [49]
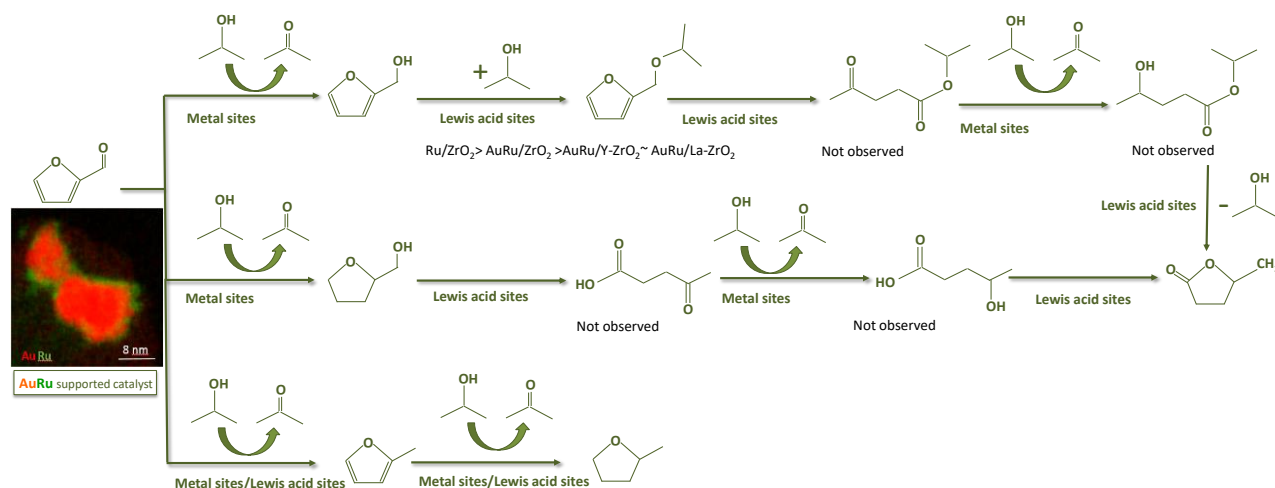
Scheme 2. Reaction pathways proposed basing on catalytic and spectroscopic evidences.

FA is then converted to isopropyl furfuryl ether following the route: Ru/ZrO_2 > $AuRu/ZrO_2$ > $AuRu/Y-ZrO_2$ ~ $AuRu/La-ZrO_2$, revealing a role of Lewis acid sites, according to Scheme 2. However, a small amount of furfural can be hydrogenated to tetrahydro furfuryl alcohol, or to 2-methyl furan on $AuRu/Y-ZrO_2$ and further to 2-methyl tetrahydrofuran on $AuRu/ZrO_2$. Over reduction by-products are not observed on $AuRu/La-ZrO_2$, indicating a possible involvement of the Lewis sites in the complete hydrogenation, given the same nature of the metal exposed sites as demonstrated by HAADF STEM, FTIR spectroscopy of adsorbed CO and XPS analyses.

As shown in Scheme 2, tetrahydro furfuryl alcohol and isopropyl-furfuryl ether can be promptly converted by Lewis acid sites into a mixture of levulinic acid and isopropyl levulinate (these compounds were not observed) through hydrolytic ring-opening reactions. These intermediates can form the corresponding 4-hydroxypentanoates (not observed) by H-transfer catalysed by the metal sites and form GVL trough lactonization.

Acetonitrile adsorption revealed the low acidic character of the $AuRu/La-ZrO_2$, due to the presence of two kinds of Lewis acid sites, with different acidic strength, i.e. La^{3+} < Zr^{4+}. This feature can explain the lowest selectivity to GVL shown by this catalyst, on which FA is mainly produced. Conversely, Zr^{4+} sites with lower acidic strength than on pure ZrO_2, are present on the Y-doped catalyst. These Y^{3+} modified Lewis sites are able to catalyze selectively the production of GVL over the $AuRu/Y-ZrO_2$ catalyst.

4. Conclusions

The presence of Ru metallic sites, whose abundance and electronic properties are modified by gold, improved the catalytic activity of AuRu supported nanoparticles in furfural hydrogenation by H-transfer with 2-propanol. Moreover, gold influences the stability of the catalysts under reaction conditions.

The interaction between the catalysts and the hydrogen donor has been carefully investigated and it was shown that 2-propanol interacts with the PVA chains, resulting in an enhanced accessibility of the Ru sites and promoted transfer hydrogenation reactions.

The Lewis acidity modified by Y^{3+} of the AuRu/Y-ZrO$_2$ is mandatory to selectively produce GVL.

References

1   R. Mariscal, P. Maireles-Torres, M. Ojeda, I. Sádaba and M. López Granados, *Energy Environ. Sci.*, 2016, 9, 1144–1189.

2   X. Li, P. Jia and T. Wang, *ACS Catal.*, 2016, **6**, 7621–7640.

3   J. P. Lange, E. Van Der Heide, J. Van Buijtenen and R. Price, *ChemSusChem*, 2012, 5, 150–166.

4   J. J. Bozell and G. R. Petersen, *Green Chem.*, 2010, 12, 539–554.

5   B. Sreedhar, V. Shasikala, A. H. Padmasri, B. M. Nagaraja, K. S. Rama Rao, V. Siva Kumar and B. David Raju, *Catal. Commun.*, 2003, **4**, 287–293.

6   Y.-L. Zhu, H.-W. Xiang, Y.-W. Li, H.-Y. Zheng, Z.-Q. Bai, C.-H. Zhang and B.-T. Teng, *J. Mol. Catal. A Chem.*, 2005, **246**, 18–23.

7   S. Zhu, Y. Xue, J. Guo, Y. Cen, J. Wang and W. Fan, *ACS Catal.*, 2016, **6**, 2035–2042.

8   J. Iglesias, J. A. Melero, G. Morales, M. Paniagua, B. Hernández, A. Osatiashtiani, A. F. Lee and K. Wilson, *Catal. Sci. Technol.*, 2018, **8**, 4485–4493.

9   J. Xu, F. Liu, A. Wang, B. Qiao, S. Miao, Y. Su, H. Sun, L. Li, T. Zhang, Y.-T. Cui, L. Li, R. Lang, F. Jerome and Q. Liu, *Green Chem.*, 2018, **20**, 1770–1776.

10   T. Mizugaki, T. Yamakawa, Y. Nagatsu, Z. Maeno, T. Mitsudome, K. Jitsukawa and K. Kaneda, *ACS Sustain. Chem. Eng.*, 2014, **2**, 2243–2247.

11   K. Huang, Z. J. Brentzel, K. J. Barnett, J. A. Dumesic, G. W. Huber and C. T. Maravelias, *ACS Sustain. Chem. Eng.*, 2017, **5**, 4699–4706.

12   D. M. Alonso, S. G. Wettstein and J. A. Dumesic, *Green Chem.*, 2013, 15, 584–595.

13   E. I. Gürbüz, J. M. R. Gallo, D. M. Alonso, S. G. Wettstein, W. Y. Lim and J. A. Dumesic, *Angew.*

Chemie - Int. Ed., 2013, **52**, 1270–1274.

14   L. Bui, H. Luo, W. R. Gunther and Y. Román-Leshkov, *Angew. Chemie - Int. Ed.*, 2013, **52**, 8022–8025.

15   S. H. Pang and J. W. Medlin, *ACS Catal.*, 2011, **1**, 1272–1283.

16   R. E. Palmer, N. Jian, A. Villa, N. Dimitratos, C. R. A. Catlow, A. Chutia, P. P. Wells, C. E. Chan-Thaw, S. M. Rogers, M. Perdjon and A. Thetford, *ACS Catal.*, 2017, **7**, 2266–2274.

17   W. Wang, A. Villa, C. Kübel, H. Hahn and D. Wang, *ChemNanoMat*, 2018, **4**, 1125–1132.

18   S. Wang, V. Vorotnikov and D. G. Vlachos, *ACS Catal.*, 2015, **5**, 104–112.

19   R. Fang, H. Liu, R. Luque and Y. Li, *Green Chem.*, 2015, **17**, 4183–4188.

20   P. Panagiotopoulou and D. G. Vlachos, *Appl. Catal. A Gen.*, 2014, **480**, 17–24.

21   J. Kijeński, P. Winiarek, T. Paryjczak, A. Lewicki and A. Mikolajska, *Appl. Catal. A Gen.*, 2002, **233**, 171–182.

22   L. Robert Baker, V. V. Pushkarev, K. An, G. A. Somorjai, G. Kennedy and N. Musselwhite, *J. Colloid Interface Sci.*, 2012, **392**, 122–128.

23   A. Wang, X. Y. Liu, C. Y. Mou and T. Zhang, *J. Catal.*, 2013, **308**, 258–271.

24   G. J. Hutchings, *Catal. Today*, 2014, **238**, 69–73.

25   C. Louis, *Catalysts*, 2016, **6**, 110.

26   A. Villa, D. Wang, D. S. Su and L. Prati, *Catal. Sci. Technol.*, 2015, 5, 55–68.

27   K. I. Hadjiivanov and G. N. Vayssilov, *Adv. Catal.*, 2002, **47**, 307–511.

28   C. Morterra, V. Bolis, B. Fubini, L. Orio and T. B. Williams, *Surf. Sci.*, 1991, **251**–**252**, 540–545.

29   E. Guglielminotti, F. Boccuzzi, M. Manzoli, F. Pinna and M. Scarpa, *J. Catal.*, 2000, **192**, 149–157.

30   M. Manzoli, V. N. Shetti, J. A. L. Blaine, L. Zhu, D. Isrow, V. Yempally, B. Captain, S. Coluccia, R. Raja and E. Gianotti, *Dalt. Trans.*, 2012, **41**, 982–989.

31   J.-C. Lavalley, K. Hadjiivanov, M. Che, F. Maugé, J. Lamotte and J. Saint-Just, *J. Catal.*, 2002, **176**, 415–425.

32   P. Hollins, *Surf. Sci. Rep.*, 1992, **16**, 51–94.

33   D. Wang, X. Cui, Q. Xiao, Y. Hu, Z. Wang, Y. M. Yiu and T. K. Sham, *AIP Adv.*, 2018, **8**, 065210.

34   J. Sha, S. Paul, F. Dumeignil and R. Wojcieszak, *RSC Adv.*, 2019, **9**, 29888–29901.

35   C. M. Olmos, L. E. Chinchilla, A. Villa, J. J. Delgado, H. Pan, A. B. Hungría, G. Blanco, J. J. Calvino, L. Prati and X. Chen, *Appl. Catal. A Gen.*, 2016, **525**, 145–157.

36   E. D. Park and J. S. Lee, *J. Catal.*, 1999, **186**, 1–11.

37   X. Zhang, H. Wang and B. Q. Xu, *J. Phys. Chem. B*, 2005, **109**, 9678–9683.

38   S. Ardizzone, M. G. Cattania, P. Lazzari and P. Lugo, *Colloids Surfaces A Physicochem. Eng. Asp.*, 1994, **90**, 45–54.

39   D. J. Morgan, *Surf. Interface Anal.*, 2015, **47**, 1072–1079.

40   S. Esposito, B. Silvestri, V. Russo, B. Bonelli, M. Manzoli, F. A. Deorsola, A. Vergara, A. Aronne and M. Di Serio, *ACS Catal.*, 2019, **9**, 3426–3436.

41   Y. Suchorski, R. Wrobel, S. Becker, A. Opalińska, U. Narkiewicz, M. Podsiadly and H. Weiss, in *Acta Physica Polonica A*, 2008, vol. 114, p. S-125-S-134.

42   Y. Uwamino, T. Ishizuka and H. Yamatera, *J. Electron Spectros. Relat. Phenomena*, 1984, **34**, 67–78.

43   T. Gougousi and Z. Chen, *Thin Solid Films*, 2008, **516**, 6197–6204.

44   P. Pisecny, K. Husekova, K. Frohlich, L. Harmatha, J. Soltys, D. Machajdik, J. P. Espinos, M. Jergel and J. Jakabovic, in *Materials Science in Semiconductor Processing*, Pergamon, 2004, vol. 7, pp. 231–236.

45   H. Knoezinger and H. Krietenbrink, *J. Chem. Soc. Faraday Trans. 1 Phys. Chem. Condens. Phases*, 1975, **71**, 2421–2430.

46   K. F. Purcell and R. S. Drago, *J. Am. Chem. Soc.*, 1966, **88**, 919–924.

47   M. J. Gilkey, P. Panagiotopoulou, A. V. Mironenko, G. R. Jenness, D. G. Vlachos and B. Xu, *ACS Catal.*, 2015, **5**, 3988–3994.

48   B. Hernández, J. Iglesias, G. Morales, M. Paniagua, C. López-Aguado, J. L. García Fierro, P. Wolf, I. Hermans and J. A. Melero, *Green Chem.*, 2016, **18**, 5777–5781.

49   F. Menegazzo, T. Fantinel, M. Signoretto, F. Pinna and M. Manzoli, *J. Catal.*, 2014, **319**, 61–70.